2D label-free imaging of resonant grating biochips in ultraviolet

Kristelle Bougot-Robin, Jean-Luc Reverchon, Michel Fromant, Laurent Mugherli, Pierre Plateau, Henri Benisty

2D label-free imaging of resonant grating biochips in ultraviolet

K. Bougot-Robin, [1,*], J-L. Reverchon[1], M. Fromant[2], L. Mugherli[2], P. Plateau[2], H. Benisty[3]

[1]*Thales Research & Technology, 1 avenue Fresnel, Campus Polytechnique, 91767 Palaiseau, France*
[2]*Laboratoire de Biochimie, Ecole Polytechnique, CNRS, 91128 Palaiseau Cedex, France*
[3]*Institut Optique Graduate School, 2 avenue Fresnel, Campus Polytechnique, 91127 Palaiseau, France*
**kristelle_robin@yahoo.fr*

Abstract: 2D images of label-free biochips exploiting resonant waveguide grating (RWG) are presented. They indicate sensitivities on the order of 1 pg/mm^2 for proteins in air, and hence 10 pg/mm^2 in water can be safely expected. A 320×256 pixels Aluminum-Gallium-Nitride-based sensor array is used, with an intrinsic narrow spectral window centered at 280 nm. The additional role of characteristic biological layer absorption at this wavelength is calculated, and regimes revealing its impact are discussed. Experimentally, the resonance of a chip coated with protein is revealed and the sensitivity evaluated through angular spectroscopy and imaging. In addition to a sensitivity similar to surface plasmon resonance (SPR), the RWGs resonance can be flexibly tailored to gain spatial, biochemical, or spectral sensitivity.

OCIS codes: (280.1415) Biological sensing and sensors; (310.2785) Guided wave; (050.5745) Resonance domain; (300.1030) Absorption; (170.0110) Imaging systems

References

1. A. Hessel, and A. A. Oliner, "A New Theory of Wood's Anomalies on Optical Gratings," Appl. Opt. **4**(10), 1275–1297 (1965).
2. U. Fano, "Effects of Configuration Interaction on Intensities and Phase Shifts," Phys. Rev. **124**(6), 1866–1878 (1961).
3. I. E. Araci, S. B. Mendes, N. Yurt, S. Honkanen, and N. Peyghambarian, "Highly sensitive spectroscopic detection of heme-protein submonolayer films by channel integrated optical waveguide," Opt. Express **15**(9), 5595–5603 (2007).
4. M. Nakkach, P. Lecaruyer, F. Bardin, J. Sakly, Z. Ben Lakhdar, and M. Canva, "Absorption and related optical dispersion effects on the spectral response of a surface plasmon resonance sensor," Appl. Opt. **47**(33), 6177–6182 (2008).
5. I. D. Block, P. C. Mathias, N. Ganesh, S. I. Jones, B. R. Dorvel, V. Chaudhery, L. O. Vodkin, R. Bashir, and B. T. Cunningham, "A detection instrument for enhanced-fluorescence and label-free imaging on photonic crystal surfaces," Opt. Express **17**(15), 13222–13235 (2009).
6. I. D. Block, P. C. Mathias, S. I. Jones, L. O. Vodkin, and B. T. Cunningham, "Optimizing the spatial resolution of photonic crystal label-free imaging," Appl. Opt. **48**(34), 6567–6574 (2009).
7. R. B. M. Schasfoort, and A. McWhirter, in *Handbook of surface plasmon resonance* (R.B.M Schasfoort and A. J. Tudos, RSC Publishing Enschede, Netherlands, 2007), Chap. 3.
8. P. Y. Li, B. Lin, J. Gerstenmaier, B. T. Cunningham, "A new method for label-free imaging of biomolecular interactions," Sens. Act. Chem. **99**(1), 6–13 (2004).
9. E. M. Yeatman, "Resolution and sensitivity in surface plasmon microscopy and sensing," Bios. Bioelec. **11**(6-7), 635–649 (1996).
10. N. Ganesh, I. D. Block, and B. T. Cunningham, "Near ultraviolet-wavelength photonic-crystal biosensor with enhanced surface-to-bulk sensitivity ratio," Appl. Phys. Lett. **89**(2), 023901 (2006).
11. K. Robin, J. L. Reverchon, L. Mugherli, M. Fromant, P. Plateau, and H. Benisty, "Detection of biological macromolecules on a biochip dedicated to UV specific absorption," Bios. Bioelec. **24**(6), 1585–1591 (2009).
12. J. L. Reverchon, J. A. Robo, J. P. Truffer, J. P. Caumes, I. Mourad, J. Brault, and J. Y. Duboz, "AlGaN-based focal plane arrays for selective UV imaging at 310nm and 280nm and route toward deep UV imaging", Proc. SPIE **6744** (2007).

#125895 - $15.00 USD Received 26 Mar 2010; revised 5 May 2010; accepted 6 May 2010; published 14 May 2010

13. K. Robin, J. L. Reverchon, L. Mugherli, M. Fromant, and H. Benisty, "Biodetection of DNA and proteins using enhanced UV absorption by structuration of the chip surface", Proc. SPIE **7188**-04 (2009).
14. L. Li, "Formulation and comparison of two recursive matrix algorithms for modeling layered diffraction gratings," J. Opt. Soc. Am. A **13**(5), 1024–1035 (1996).
15. A. David, "High efficiency GaN-based LEDs: light extraction by photonic crystals," Ann. Phys. (Paris) **31**(6), 1–235 (2006).
16. F. David, Edwards, "Silicon (Si)" in *Handbook of optical constants of Solids*, E. D. Palik ed.(Academic, Press, 1985).
17. V. Brioude, and O. Parriaux, "Normalised analysis for the design of evanescent-wave sensors and its use for tolerance evaluation," Opt. Quant. Elec. **32**(6/8), 899–908 (2000).
18. D. Bahatt, J. E. Cahill, K. Nishikida, E. G. Picozza, P. G. Saviano, D. H. Tracy, and Y. Wang, "Optical resonance analysis system", US patent 7251085, (2007).
19. E. Özkumur, J. W. Needham, D. A. Bergstein, R. Gonzalez, M. Cabodi, J. M. Gershoni, B. B. Goldberg, and M. S. Unlü, "Label-free and dynamic detection of biomolecular interactions for high-throughput microarray applications," Proc. Natl. Acad. Sci. U.S.A. **105**(23), 7988–7992 (2008).

1. Introduction

For biological recognition assays, optical detection methods based on guided waves probing biological layers find their use in drug screening, diagnostic, pollution, defense...

These sensing methods are generally based on the real part of the optical index Δn. Resonant waveguide gratings (RWGs) act much like surface plasmon resonance (SPR) does, the grating coupling of the former replacing the tunnel coupling of the latter. In both cases, the largest sensitivity is obtained at near-resonance wavelength $\lambda \approx \lambda_r$, where the incident wave's in-plane wavevector nearly matches the guided mode wavevector characterized by its dispersive effective index n_{eff}. Equation (1) gives this condition for a grating of period Λ in an ambient medium of index n_a, at a coupling angle θ, and for the m^{th} diffracted order.

$$n_{\text{eff}}(\lambda_r, \theta_r) = n_a \sin 0(\theta) + m\frac{\lambda_r}{\Lambda} \tag{1}$$

Resonance phenomena are revealed by reflectivity anomalies of R(λ,θ) (Fano shapes [1,2]) well known to provide enhanced sensitivity by measuring either R(λ) or R(θ). In ultraviolet, characteristic absorption lines exist for protein (λ = 280 nm) and DNA (λ = 260 nm), whose interest for the biochip detection format is scarcely addressed. In general, absorption may influence guided wave propagation [3,4], giving signals at the guide end (interferometric techniques, attenuated total reflection…), or it may act through a modified resonant coupling behaviour. Absorption being calibrated and less sensitive to temperature, it may be more robust to quantitative analysis.

Methods with beams of limited optical etendue, e.g. lasers, are limited to a single spot biological analysis. In a setup dedicated to imaging, introducing a modest beam etendue makes resonance condition compatible with retrieval of spatial information such as the local diffraction efficiency η(*x*,*y*,λ,θ) around a wavelength λ and an incidence angle θ [5,6]. The 2D images can therefore be used for multiplexed biological detection (Fig. 1(c)). This is used in recently commercialized SPR imaging techniques [7]. Dielectric resonant waveguide grating imaging (RWGi) features a similar degree of field concentration and opens new opportunities for biochips. It has mainly been studied through spectro-imaging devices, acquiring 1D line intensities I(*x*,λ) and searching the resonant λ_r for each abscissa *x* [8]. We present here full 2D RWGi data avoiding the opto-mechanical *y* scan.

Sensitivity directly follows the modal decay length. In the visible, the propagation length of an Au surface plasmon is ~10 µm. Therefore, RWGs adjusted to a ~50 µm decay length [9] could be more sensitive with a resolution compatible with spots in current assays. Mitigation from all optogeometric parameters should of course be considered: for instance, the tighter angular filtering for larger decay length may diminish the signal-to-noise ratio.

We targeted the domain around 280 nm, where proteins strongly absorb, which may play a role for the sensitivity [3,4] and ideally enhance it in cases of low index contrasts. The UV domain is not attainable with currently used plasmons on Au or Ag, and only UV permits

#125895 - $15.00 USD Received 26 Mar 2010; revised 5 May 2010; accepted 6 May 2010; published 14 May 2010

protein label-free absorption sensing. The short wavelength λ also increases the ratio ℓ/λ where ℓ is a given biological layer effective thickness, resulting in better sensitivity [10].

2. Resonant grating biochip imaging

In line with our previous work on multilayer UV sensing, a reflective set-up, Fig. 1(a,b), is chosen [11]. The biochip pattern consists of an array of biological spots of typical size 140 µm, and a distance from center to center of 400 µm, Fig. 1(c). In the biochip imaging version of the set-up, Fig. 1(b), the biochip is illuminated with a continuous Xenon source. A monochromator is inserted in order to select the resonant wavelength associated with the chosen angle. The signal is measured with a spectrally selective AlGaN array [12]. In view of experiments in solution whereby a larger effect of absorption presents additional opportunities, AlGaN components keep all possibilities open, being intrinsically selective in the absorption window (λ_{max} = 280 nm, Δλ ~20 nm). Fluorescence signals from tryptophan (300-350 nm) are filtered. The ~0.5 mW flux of typical AlGaN LEDs shall increase in the near future, to possibly replace Xenon lamps in portable instruments. With the set-up sketched in Fig. 1(a), a spectroscopic characterisation can also be performed: a fibered spectrometer is used in this case, instead of a 2D array detector and the monochromator is removed.

The biochip structure (Fig. 2) consists of a waveguide, with a coupling grating on its surface assisted by a UV mirror just beneath. For imaging applications, orders diffracted close to the chip's normal are privileged. But if one dares using a non specular order, images are on dark field, which may prove advantageous to reject photons from non grating regions. For biochips imaging, a layer-induced reflectivity contrast *C* arises. It can be measured from the change of spot reflectivity R_{spot} vs. bare chip reflectivity R_{chip}. In a limit case of contrast induced only by absorption (Δn = 0 due to protein and buffer matched indices for instance), this contrast can also be quantified as a specific enhancement factor Γ_{abs}, according to the following expressions:

$$C = \frac{\Delta R}{R} = \frac{R_{chip} - R_{spot}}{R_{chip}}, \qquad \Gamma_{abs} = C/\alpha\ell \tag{2}$$

where $\alpha\ell$ gives the bound analyte layer absorption.

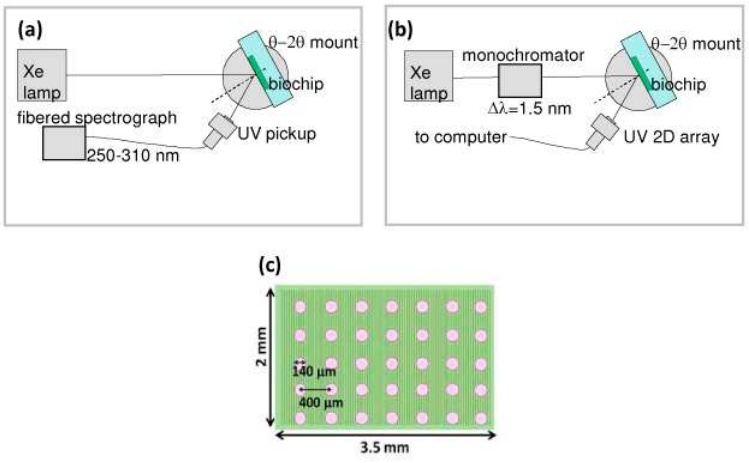

Fig. 1. Schemes of detection instrumentation (a) for spectroscopy characterization where the large spectrum reflected signal is measured through an optical fiber and (b) for the imaging set-up, where the light is filtered through a monochromator and measured with a UV 2D detector; (c) Top view of the 2D biochip with spots of typical size 140 µm with center to center distance of 400 µm.

#125895 - $15.00 USD Received 26 Mar 2010; revised 5 May 2010; accepted 6 May 2010; published 14 May 2010

The sensitivity optimization of a RWG biochip has been presented in [13]. To fit with mainstream technologies, the materials chosen are silicon nitride (SiN) on silica (SiO_2), on a silicon substrate (Si). The chip designed here has a period Λ = 270 nm, which enables to have two different diffracted orders under diffraction cut-off in the ambient medium. Diffraction efficiencies $\eta(\lambda,\theta)$ in TE polarization are calculated thanks to a scattering matrix approach [14,15], taking into account refractive index dispersion laws. For the near metallic Si mirror (n_{280nm} = 2.97+5.3i, R = 75%), we use tabulated values [16], whereas for SiO_2 and SiN, we use our own 190-800 nm ellipsometric measurements giving the indices $n_{SiO2,\ 280\ nm}$ = 1.495 and $n_{SiN,\ 280\ nm}$ = 1.895+0.0001i. The coating protein is here the methionyl-tRNA synthetase (MetRS) of mass 64 kDa. From an optics point of view, it is representative of other proteins, and can be simply modeled by a refractive index n and a thickness ℓ. Its dispersion law is fitted with a two-Lorentz-oscillators model, one centred at 280 nm from the aromatic amino acids (tryptophan, tyrosine, phenylalanine, all containing an aromatic ring C_6H_x) and the other at 190 nm for peptidic bond absorption (–C(=O)NH–). The protein optical index n_{280nm} = 1.49 + 0.006i translates into a single-pass absorption $\alpha\ell = 0.35\times10^{-3}$ for a 2.5 nm thick typical layer (2×10^{12} molecules/cm^2, with absorptivity $\varepsilon_{280nm} = 1.72\times10^{-2}$ cm^2/µg).

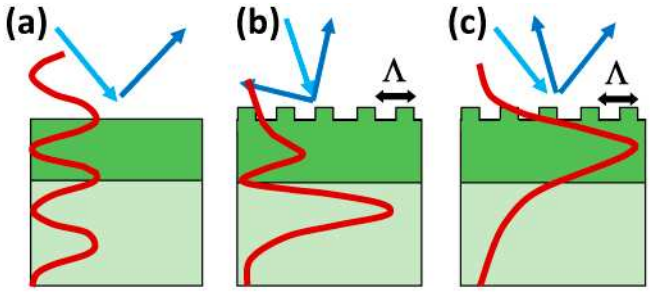

Fig. 2. Side view and electric field profiles first for (a) a non-corrugated chip showing the λ/2 SiN thickness and 3λ/4 SiO_2 layer optical thicknesses (b) for the SiO_2 mode and (c) for the SiN mode.

Figure 2 gives a schematic profile of (a) the stationary wave without corrugation, (b) the SiO_2 mode and (c) the SiN guided mode profiles (TE polarisation). The SiN guiding layer has an optical thickness around $\lambda/2n$ (70 nm) providing to its mode profile a fair leakage in the outer medium, a key aspect for sensitivity to the biological layer [17]. We then select a $3\lambda/4n$ SiO_2 optical thickness (140 nm) to have maxima of the nonresonant stationary wave at both waveguide interfaces. This thickness naturally keeps the SiN guided mode far from the mirror and reduces associated losses in silicon. This "vertical" engineering maximizes the coupling of light to the guided wave, and minimizes in turn the demand on grating etch depth.

To match the experimental data shown in Section 3, we model the signal of a 2.5 nm-thick MetRS protein monolayer, namely a 2000 pg/mm^2 density. The reflectivity profiles without or with biological layer, as well as the induced reflectivity induced contrast C are given in Fig. 3(a) at θ = 39° (resonance at ~280 nm). The chip TE reflectivity map $R_o(\lambda,\theta)$ in Fig. 3(b), evidences the scars of the SiO_2 and SiN modes. We added to it contours of iso-diffraction angle at −1st order, and the Littrow line (whereby $\theta_{-1}=\theta_0$). The entire contrast map in Fig. 3(c), highlights the higher sensitivity of the SiN mode to the protein layer. The main features induced by the protein are a shift of λ_r and a lower diffraction efficiency due to protein absorption.

The UV domain gives the opportunity to sense absorption of the biomolecules. To assess the role of absorption and real part of the index whose contributions cannot be separated, we assume for simplicity a hypothetical biological layer having a nondispersive index of 1.49+0.06i and we refer to Fig. 4. The layer considered here is therefore 10 times more absorbing than the MetRS protein, and would represent a protein made of 100% tryptophan at

#125895 - $15.00 USD Received 26 Mar 2010; revised 5 May 2010; accepted 6 May 2010; published 14 May 2010

280 nm. This example is also directly valid for the contrast obtained in air with DNA, or can be used to infer the trend with an ambient medium different from air, which will be explained further. Focusing on the steep and nearly linear falling edge of R(λ), the contrast around resonance *C* has the general form $\Delta n\ell F + g\alpha\ell$. The first term is a "reactive" shift dictated by the path difference $\Delta n\ell$ and by the finesse $F=\lambda/\Delta\lambda$. It is maximal on the edges of R(λ), as can be seen from Fig. 3(a) (the slope of these edges scales like *F,* the peak shift scales like $\Delta n\ell$).

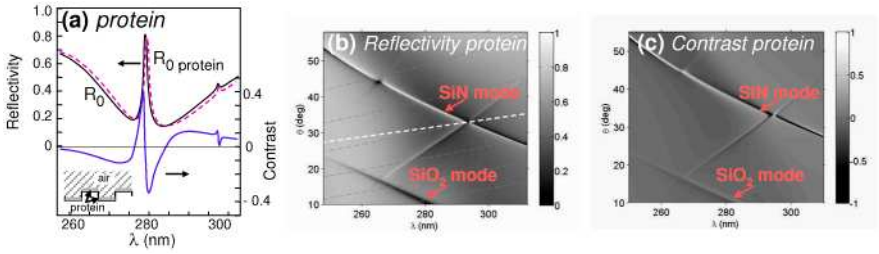

Fig. 3. (a) Reflectivity profile of the chip R_0 for a θ = 39° incidence angle without (solid line) and with a MetRS protein layer (dashed line); the bottom graph is the contrast C referred to the right side scale for this air ambient; (b) R (λ,θ) reflectivity map evidencing SiO_2 and SiN modes and (c) Similar map of reflectivity induced contrast C(λ,θ); the SiN mode strongly interacts with the biological layer.

The second term, dictated by absorption, has several components. The nonresonant one is a downward shift depending on the intensity of the stationary wave (Fig. 2(a)) at the absorber location: it is in the range of 0 to $4\alpha\ell$ (Γ_{abs} = 0 to 4) provided R_{chip} is not too low [11] and could be assumed to be weakly wavelength-dependent for our thin structures. But this second term also has here resonant components that we render as a stronger $g(\lambda)$ dependence, associated with resonance damping. Due to the resonance, the regime obtained depends on the competition between RWG's weak intrinsic losses and the equally weak losses of the biological layer.

However, if the RWG has a positive resonance peak on a lower background, as is the case in reality, Fig. 3(a), we can outline the various subtleties arising on the obtained signals through our hypothetical layer model, as shown in Fig. 4. Figure 4(a) shows the reflectivity of a bare chip (black solid line) and its modification for the n = 1.49+0.06i layer (dotted line). We also include the elementary cases of n = 1.49+0i (dashed line) and n = 1.0+0.06i (dash-dotted line), i.e., the "absorption only" effect. Of course, the spectra are close together, so it is convenient to refer to the contrast Fig. 4(b) with the three cases (1.49+0.06i, 1.49+0i and 1+0.06i). It is seen that with the resonance degree and absorption considered here, the contrast induced by the sole absorption is 0.1, peaking at resonance, and it is clearly outscored by the derivative-shaped index signal. The absorption spectral shape also shows that the non resonant absorption cannot be ignored to evaluate this term even with our finesse F ~140. This may stem from the weaker overlap of the guided mode compared to the ideal overlap of the standing wave (Fig. 2).

For the present air ambient, the strong index-induced contrast (n = 1.49+0i) represents the main signal. The combination with the absorption effect nevertheless causes a sizable asymmetry of the contrast spectral shape, with a low wavelength enhancement and a long wavelength depletion in the present configuration (in the converse case of an initial reflectivity dip, the opposite would occur). Here the asymmetry causes the absolute |C| peak values to be in a 3:2 ratio. This would be still detectable without much instrumental accuracy.

However, if we extrapolate, absorption discrimination for usual protein with 0-10% tryptophan content would require very accurate instrumentation able to determine a few percent difference in extreme |C| values. Signals would still be above noise, as we shall detail in the next paragraphs, but they could be obscured by any fluctuation, e.g. in real index contribution.

#125895 - $15.00 USD Received 26 Mar 2010; revised 5 May 2010; accepted 6 May 2010; published 14 May 2010

These conclusions are widely changed if a different ambient medium is used, e.g. water with n_a = 1.39 at 280 nm, or even a higher index. Then, the $\Delta n\ell$ contribution plummets, and the possibility to detect the small signals, characteristic of layer absorption, would demand only tight optical control of the set-up, but would be far less jeopardized by signals from real index fluctuations related to the biological aspects of actual assays. Let us give an estimate of the sensitivity in this context, as it is a key issue for label-free real time biosensors, e.g., the popular ones exploiting SPR.

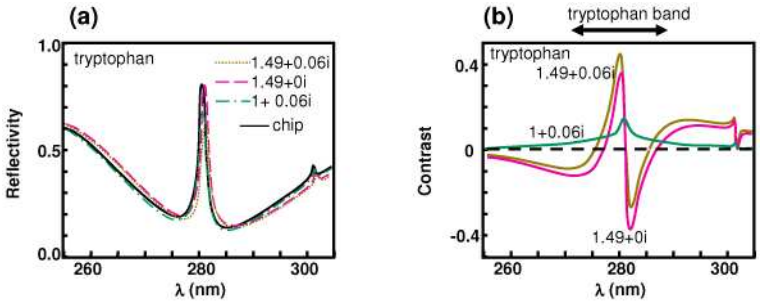

Fig. 4. (a) Reflectivity modification for various hypothetical nondispersive top layers: the bare chip is the solid black line, the three other cases are:"tryptophan layer" (dotted line, n = 1.49+0.06i), "nonabsorbing layer" (dashed line n = 1.49+0i) and "pure absorbing medium" (dash-dotted n = 1+0.06i) ; (b) Induced reflectivity contrast C(λ) for the three cases. These RWG reflectivity contrasts would be further modulated by the absorption spectra (tryptophan band around λ = 280 nm indicated).

To evaluate sensitivity in the different medium in view of biodetection, it is important to consider instrumental resolution, to have a sufficient flux. We consider here a spectral width Δλ = 1.5 nm, and an angular width of Δθ = 0.6° at half maximum. These optical limitations are taken into account by a convolution of the reflectivity with a Gaussian function for both variables. For the air as ambient medium, the large index contrast with the protein leads to a resonant contrast C_{RWG} comprised in the interval [−0.38;+0.33] for a 2000 pg/mm^2 monolayer density. The contrast in air is then decreased to the interval [−0.18;+0.22]. For a detection limit set by $\Delta R = 2\times10^{-4}$ (usual noise-limited detection criteria after averaging on 10 successive images and 10 pixels of biological spot), the limit sensitivity s_{lim} for this air ambient (Δn regime) is found in principle around 2 pg/mm^2 (with the provisions of fluctuations mentioned above). Detection in air addresses applications with dried proteins, offering label-free control of biological grafting process or end-point antigen/antibody recognition for immunological assaying.

We want to estimate the sensitivities obtained with this same chip in different media and taking angular and spectral resolution into account. Sensitivity is therefore evaluated for air (n = 1), water solution (n = 1.39), and 1:1 glycerol solution (n = 1.5). Reflectivity spectrum as well as reflectivity induced contrast are given in Fig. 5. For air, the real part of the optical index contribution is largely dominating. In the case of a water solution, n = 1.39, the index contrast is reduced from Δn = 0.495 to Δn = 0.105. The small index difference results in a mainly positive contrast.

#125895 - $15.00 USD Received 26 Mar 2010; revised 5 May 2010; accepted 6 May 2010; published 14 May 2010

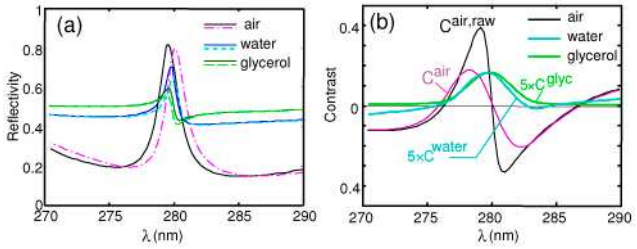

Fig. 5. (a) Reflectivity for different ambient media without (solid line) and with (dashed line) protein monolayer; for a θ = 39° incidence angle; (b) Induced reflectivity contrast C(λ) for the three cases, taking into account instrumental resolution Δθ = 0.6° and Δλ = 1.5 nm.

Taking into account instrumental resolution, sensitivity in water is therefore expected to be about 5 times lower (Fig. 5(b)) and we then expect s_{lim} ~10 pg/mm^2.For a 1:1 glycerol/water solution, absorption would is now clearly the major contribution to the signal, resulting in an exclusively positive contrast. Figure 5(b) underlines that the contrast maximum value is similar to that in water solution.

With the chip presented here, and if, as hinted above only the absorption is considered (e.g. thanks to a 1:1 glycerol/water index-matching solution) the expected limit sensitivity is similar to the one obtained in water and becomes, for the extinction coefficient of MetRS (n ~1.49+0.006i), s_{lim} ~10 pg/mm^2. We remind that the interest of absorptive detection is to be insensitive to the degree of folding of the protein. Furthermore, the use of such an absorption contrast is also adequate for nucleic acids (DNA) detection, where absorptivity ε is roughly ten times larger than that of protein, thus leading to recover the limit sensitivity figures mentioned earlier, namely s_{limDNA} = 1 pg/mm^2. Note that the chip used here is dedicated to detection in air. Sensitivity could probably be further increased by optimizing the chip for different ambient medium. Obtained sensitivities are therefore suitable for realtime detection in microarrays format [18].

Let us now compare with SPR performances. The generally accepted SPR imaging performance in water is s_{lim} ~10 pg/mm^2 and thus levels with our typical value for a water buffer. Our 1/λ wavelength scaling advantage is still balanced by more favorable optogeometric conditions available in SPR: the maximum TM field at the surface, the higher flux of visible LEDs, and the almost constant $n_{eff}(\lambda)$ law of the plasmon, thus much more easily matched with a prism in Kretschmann mount than the guided mode dispersion described in Eq. (1) [19].

3. Experimental results

3- 1 Chip and biological preparation

Chip fabrication involves the following steps. Silica is first deposited by PECVD (Plasma Enhanced Chemical Vapor Deposition) on a silicon substrate, followed by a silicon nitride PECVD deposit, which supports the RWG guided wave. To couple the guided wave, a "patched" 2×2.8 mm^2 area of gratings of period Λ = 270 nm is defined by e-beam lithography. To relax stitching requirements, the grating is divided in 400×400 μm^2 writing fields to which the biological spots will be further aligned. In the e-beam process, PMMA is spin-coated, exposed and developed, and a 20 nm-thick SiN etch using a SF_6 reactive ion etching (RIE) process is made before removing PMMA by an O_2 RIE step.

#125895 - $15.00 USD Received 26 Mar 2010; revised 5 May 2010; accepted 6 May 2010; published 14 May 2010

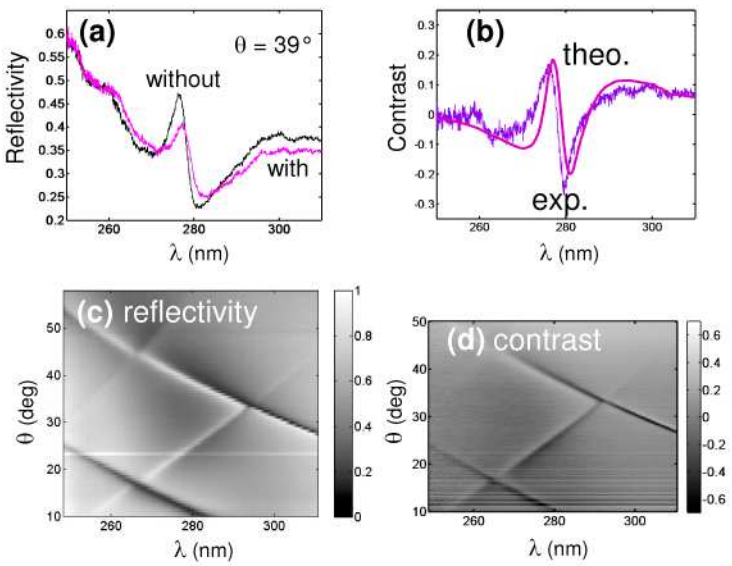

Fig. 6. Experimental data to be compared with Fig. 3. (a) Spectra R(λ) at θ = 39° without and with a 2.5 nm protein layer; (b) Comparison at θ = 39°of experimental and theoretical contrast, i.e. C^{air} of Fig. 5(b), here on the full 250-310 nm scale; (c) (θ,2θ) Chip spectroscopic characterization map. (d) Contrast map C(λ,θ) for angles 10° to 50° (a finer angular scan than Fig. 6(c) was used).

The entire biological preparation process is detailed in [11]. To retrieve the same surface chemistry as in our previous process, a 5-nm-thick PECVD silica layer is added on the structured chip. Biological spots (140 µm diameter, 400 µm pitch) are defined through a photolithography step. The next step is a silanization by chemical vapor deposition of the 3-aldehydopropyltrimethoxysilane (APTMS) molecule. This linker directly reacts with oxygen bonds of the surface. After removing the Shipley photoresist with acetone, the silanized spots may readily immobilize the proteins by reacting with their amino group. Our process results in homogeneous spots of the MetRS protein of monolayer thickness (advantageous in comparison with classical droplet spotting methods). We use a step by step characterization through atomic force microscopy and 190-800 nm spectroscopic ellipsometry measurements to accurately model the chip and the biological preparation. These measurements show the presence of a 2.5 nm biological layer inside the spots, either in the grooves or on the teeth of the grating.

3-2 Spectroscopy and imaging

To get a fine understanding of image contrast, we first perform an angularly resolved spectral characterization on a bare (no protein) 2×2.8 mm^2 chip, with a signal collected at the source image, Fig. 1(a), that merges optically the several illuminated fields (gratings) within this area. We form the beam from a continuous Xenon source of spectral power density 1.5 µW/nm around 280 nm (Δλ = 1.5 nm) in an angle Δθ = 0.6°. The incidence angle θ is scanned using a θ-2θ goniometric set-up, and 250–310 nm spectra are acquired with an Acton spectrometer for each incidence angle. Acquired spectra are normalized by a direct transmission spectrum of the incident beam.

For a fine understanding of the contrast, with tighter fabrication uncertainties, we prepared a single chip with one half of the chip fully coated with proteins (uniformly without spots) and the other half without protein, just the bare grating fields. Figure 6 gives the overall results, directly comparable to Fig. 3.

Firstly, Fig. 6(c) gives the resulting zero-order reflectivity map $R_0(\theta,\lambda)$ taken in a half without protein. The very good match of the resonant features with the RWG chip model, Fig.

#125895 - $15.00 USD Received 26 Mar 2010; revised 5 May 2010; accepted 6 May 2010; published 14 May 2010

3(b), confirms the data gained by the above accurate experimental characterizations. Observed background drifts stem from normalization, due to chromatic inhomogeneities of the incident beam.

Then, spectra are acquired on the half of the chip fully covered with protein. Figure 6(a) gives the spectra of the two halves of the our chip for $\theta = 39°$. The wavelength shift is clearly seen. It remains to be seen how much of the amplitude reduction comes from the protein or from optogeometric effects (minute orientation shifts upon sample translation is suspected). Nevertheless, Fig. 6(b) shows that quantitatively, the spectral contrast C^{air} is in good agreement with the theoretical value, Fig. 5(b).

Finally, Fig. 6(d) gives the contrast map $C(\lambda,\theta)$ obtained from the pair of angularly resolved spectral scans. It compares very reasonably with Fig. 3(c), having a clear thin dark scar in the long wavelength region $\lambda > 280$ nm of the SiN mode, and a reversed bright but weak scar in the short wavelength region $\lambda < 270$ nm. The scar of the silica mode at the bottom (270–280 nm) is more marked than it should from Fig. 3(c), but the contrast signature there remains nevertheless weaker than the SiN mode signature. The relative value of the maxima and minima in the experimental $C^{air}(\lambda)$, when compared to the trends in Fig. 4 and Fig. 5, cannot conclusively provide an absorption value, we suspect that systematic calibration uncertainties are still too large at our stage to detect less than a 10% asymmetry of these extrema. Either instrumental improvements in air or experiments in water could provide the 1% asymmetry needed for protein absorption revelation.

Let us now turn to the imaging of fully similar biochips based on the use of the set-up of Fig. 2(b). For high sensitivity, images at $\lambda = 280$ nm are realized near resonance corresponding to $\theta = 39°$ here.

Figure 7(a) gives six 0^{th} order images, acquired from 37.5° to 40°, on dried proteins. Consequently, despite the protein absorption, the contrast is dominated by the real part of their optical index. In these conditions, similarly to SPR imaging, the best sensitivity is obtained on the steepest slope of the resonance curve. In this chip design, 0^{th} and -1^{st} diffracted orders can be imaged, but we shall report elsewhere on images of the latter. The success of our design is manifested by the fact that the spots of density 2000 pg/mm^2 attain a contrast C = 0.35, and therefore a limit sensitivity s_{lim} = 1.1 pg/mm^2 for a $\Delta R = 2\times10^{-4}$ detection limit. In Fig. 7(b), we give the simulated reflectivity spectrum of the chip with and without proteins. The change in resonance angle is ~0.3° for a 2.5 nm-layer of protein. In Fig. 7(c), we report the reflectivity values obtained on the images to reconstruct the spectrum depending of incidence angle. Each reflectivity value is obtained by averaging the grey level on the chip on different spot profiles, as shown in Fig. 7(c). The resulting data points are plotted in Fig. 7(d) and superimposed onto the simulated curves. The comparison confirms the shift in resonance angle induced by the protein, as well as the degree of damping of the resonance.

As seen in Section 2, when taking into account instrumental resolution, the sensitivity expected in water is 5 times lower. Therefore, a sensitivity of the order of 6 pg/mm^2 is expected with this chip design. From these results, it is therefore reasonable to say that similar sensitivity than in SPR could be obtained experimentally, namely around 10 pg/mm^2. On these images we also observe that the resonant condition of all six gratings of the upper row is shifted by about 0.5°. This is attributed to fabrication variability, resonance being highly dependent on the guide + grating parameters (thicknesses, depth, duty cycle). Consistently with our electron-beam microscopy characterization, the difference observed here is attributed to a ~5% variation in mark-space ratio of the gratings in this row. Conformal grating fabrication would limit this dependence, but the design (and mostly the grating depth) should be re-optimized adequately to retain sensitivity enhancement.

#125895 - $15.00 USD Received 26 Mar 2010; revised 5 May 2010; accepted 6 May 2010; published 14 May 2010

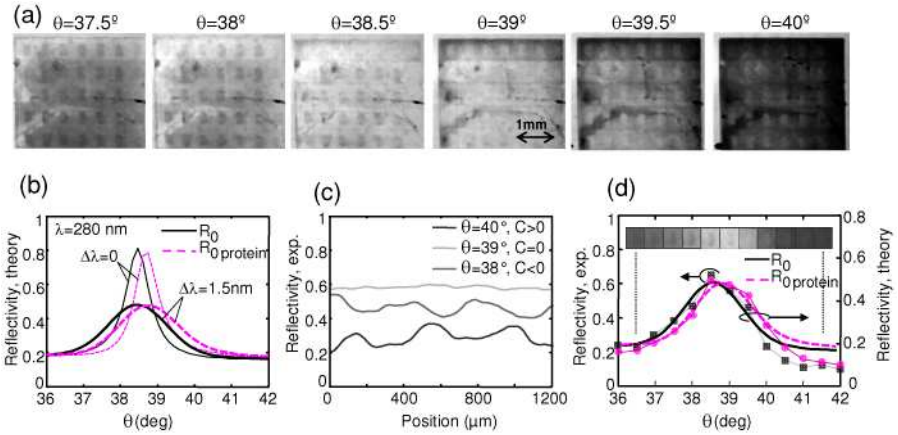

Fig. 7. (a) Images of biochip for different incidence angles from 37.5 to 40° of incidence angle. The contrast is induced by the shift of the resonance wavelength. The bar is 1 mm. (b) Theoretical reflectivity with and without protein calculated taking into account a $\Delta\lambda$ = 1.5 nm spectral resolution and $\Delta\theta$ = 1° angular aperture for sufficient incidence flux (c) Average of nine horizontal reflectivity profiles R(x) chosen in scratch-free regions of the image: they run across 3 sets of 3 spots on lines 2, 3 and 5. Three different angles profiles are plotted, illustrating positive contrast (θ = 40°, black spots on bright field), null contrast (θ = 39°), and negative contrast (θ = 38°, bright spots on dark field) and (d) Experimental reflectivity values of the images plotted for each incidence angle inside and outside biological spots, and simulated curves. An image of a single spot at each angle is also given.

4. Discussion

Imaging on resonant grating structures (RWGi) provides competitive sensitivities in comparison to the well-known SPR imaging methods [9]. SPR sensitivity is inherently limited by the nature of the metal-based plasmon and the losses in the metal.

In theory, highly resonant gratings, which sustain intermediate propagation length of 50-100 μm, can provide very high sensitivities, keeping propagation length compatible with imaging applications (engineering slow waves is needed to get more resonance without increasing spatial spread). Index sensitivity is proportional to the slope of the resonance curve, and can therefore be higher in RWGi than in SPR. However, this advantage is preserved only if spectral and angular resolutions are sufficient: sharper resonances also imply a decrease of the exploitable flux, and a lower signal/noise ratio. Therefore, it is reasonable to say that with the current low-cost large etendue / milliwatt sources such as LEDs, RWGi sensitivities similar to SPR are obtained.

But such 2D imaging techniques offer new advantages, such as the direction of diffracted orders close to the chip's normal, or the specific wavelength domain not accessible to gold-based SPR. Here, associated with new 2D AlGaN detectors, a set-up and a RWG design for UV imaging of biochips was validated, offering the possibility to exploit short wavelength and absorption of proteins around 280 nm.

Depending on the ratio $\Delta n/\alpha$, our approach can use both properties, and favour one of them through the choice of the ambient medium. The sensitivity obtained experimentally in air, s_{lim} = 1.1 pg/mm^2. Based on simulations, it translates into sensitivities of the order of s_{lim} ~10 pg/mm^2 in water or in an index-matched 1:1 glycerol/water solution where the only effect is absorption. An interesting feature of absorption sensing is its immunity to the degree of unfolding of proteins, and therefore temperature variations, unlike Δn .This RWGi option brings new parameters with sensitivities still in line with the SPR ones. An interesting case where the sole absorption effects should provide a good sensitivity is DNA, with $\varepsilon_{DNA} \sim 10\varepsilon_{proteins}$.

#125895 - $15.00 USD Received 26 Mar 2010; revised 5 May 2010; accepted 6 May 2010; published 14 May 2010

5. Conclusion

In conclusion, we present in this paper the first one-shot 2D images of label-free dielectric resonant waveguide grating biochips. Our UV imaging set-up can be used for grafting control and quantitative biological recognition for an end-point measurement in dry form. The weaker sensitivity expected in solution still remains attractive for real-time label-free detection, whereby advantages can be gained from other characteristics (wavelength, differential sensitivity to species in solution, insensitivity to folding degree,…) .

Specifically, the UV domain offers the advantages of a higher sensitivity due to the short wavelength. Absorption properties of biological molecules can also be exploited, offering interesting perspectives through reduced temperature dependency. However, a close scrutiny would be required since these two effects may not yield additive contributions in conditions other than ours. The results presented can be extended to other wavelength domains for RWGi, offering sensitivities similar to SPR, or more if a large photon flux allows tight spectral and angular filtering. The large flexibility concerning the choice of the chip parameters, optical and biological compromises highlights the interesting perspectives of RWGs for real-time imaging in a 2D array format.

Acknowledgments

The authors are grateful to P. Chavel, A. Brignon, J-P. Huignard and S. Blanquet for fruitful discussion, and to HORIBA-Jobin-Yvon for technical support and kind access to their 190-800 nm ellipsometer.

#125895 - $15.00 USD Received 26 Mar 2010; revised 5 May 2010; accepted 6 May 2010; published 14 May 2010